Article

Water Impingement Erosion of Deep-Rolled Ti64

Dina Ma [1], Ahmad Mostafa [1,2], Dmytro Kevorkov [1], Pawel Jedrzejowski [3], Martin Pugh [1] and Mamoun Medraj [1,2,*]

[1] Department of Mechanical and Industrial Engineering, Concordia University, 1455 de Maisonneuve Blvd. West, Montreal, QC H3G 1M8, Canada; E-Mails: madi121207@gmail.com (D.M.); ah_mosta@encs.concordia.ca (A.M.); kevorkov@encs.concordia.ca (D.K.); martin.pugh@encs.concordia.ca (M.P.)

[2] Mechanical and Materials Engineering, Masdar Institute, P.O. Box 54224, Abu Dhabi, UAE

[3] Rolls-Royce Canada Ltd.—Energy, 9545 Cote-de-Liesse, Dorval, QC H9P 1A5, Canada; E-Mail: pawel.jedrzejowski@rolls-royce.com

* Author to whom correspondence should be addressed; E-Mail: mmedraj@encs.concordia.ca; Tel.: +1-514-848-2424 (ext. 3146); Fax: +1-514-848-3175.

Abstract: In this work, the Liquid Impingement Erosion (LIE) performances of deep-rolling (DR) treated and non-treated Ti64 were investigated. Various erosion stages, from the incubation to the terminal erosion stages, could be observed. A full factorial design of experiments was used to study the effect of DR process parameters (Feed Rate, Spindle Velocity, Number of Passes, Pressure) on the residual stress distribution, microhardness and surface roughness of the treated Ti64 specimens. The DR-treated Ti64 specimens exhibited improved surface microhardness, surface roughness, and large magnitude of compressive residual stresses, which were attributed to the amount of cold work induced by the DR process. Although DR improved the mechanical properties of the Ti64, the results showed that the treatment has little or no effect on the LIE performance of Ti64 but different damage modes were observed in these two cases. Evolution of the erosion stages was described based on water-hammer pressure, stress waves, radial wall jetting, and hydraulic penetration modes. The initial erosion stages were mainly influenced by water-hammer pressure and stress waves, whereas the intermediate erosion stages were influenced by the combination of the four modes together. The final erosion stages contain the four modes, however the erosion was greatly driven by the radial jetting and hydraulic penetration modes, where more

material was removed. The failure mechanism of the final stages of the LIE test of both DR-treated and non-treated Ti64 was characterized as fatigue fracture. However, a brittle fracture behavior was observed in the initial and intermediate erosion stages of the DR-treated Ti64, whereas a ductile fracture behavior was observed in the non-treated Ti64. This was concluded from the micrographs of the LIE damage through different erosion stages.

Keywords: deep-rolling (DR); titanium alloys; design of experiments (DOE); liquid impingement erosion (LIE); fatigue failure; SEM; Ti64

1. Introduction

In the power generation industry, inlet fog cooling is used to cool down the turbine intake air. Gas turbine inlet air fog cooling is the most direct, cost-effective, and energy efficient solution for increasing the power output of gas turbines [1]. It is performed by spraying water into the gas turbine inlet. Some of the sprayed water droplets absorb heat from the air, through evaporation, while the remaining droplets enter the compressor as overspray to cause further cooling [2]. However, this approach leads to liquid impingement erosion (LIE) of the rotating blades in the compressor, resulting in performance degradation and service life reduction of gas turbines [3]. LIE is defined as the continuous material loss from a solid surface due to the repeated impacts of liquid drops or jets [4]. The evolution of various LIE damage stages with time is shown in Figure 1 [4–7].
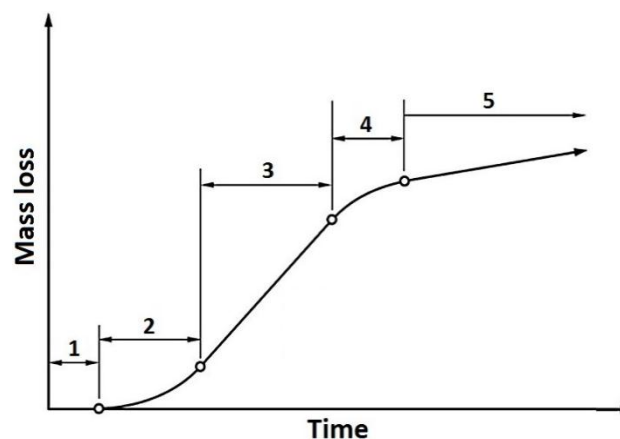

Figure 1. Evolution of LIE damage stages [4]. In sequential order: 1: incubation period; 2: acceleration period; 3: maximum rate period; 4: deceleration period; 5: terminal period.

The failure type of the eroded parts was referred to as a fatigue mechanism due to repeated impacts of the water droplets [8]. Thus, previous studies [9–13] have introduced several mechanical surface treatments as potential solutions to improve the fatigue life of specimens. Among these treatments are laser shock peening (LSP), shot peening (SP), low plasticity burnishing (LPB), and deep-rolling (DR). Mechanical surface treatments are often utilized to improve the mechanical properties, such as fatigue life, of metallic structures by developing a sufficiently deep compressive layer and favorable surface

structures on the surface of the test specimen [14,15]. For instance, LPB treatment was used to enhance the fatigue resistance of Ti64 fan blades [16–21].

Deep-rolling is a mechanical surface treatment using rolls or ball-point tools inducing deep compressive residual stresses and plastic deformations on the sample surface [13,22–24]. In contrast, in low-plasticity burnishing process load is usually applied with lower forces or pressures and mostly aims to obtain a certain surface quality with minimized surface roughness and plastic deformation [25–27]. The scope of this work is focused on the DR surface treatment.

Deep-rolling process involves controlled pressure through a smooth hydrostatically-seated hard ball or cylinder against the surface of a specimen, under a normal force sufficient to plastically deform its surface [13]. The burnishing tool is normally held in a lathe tool holder in place of the cutting tool, or can be held by any CNC machine or an industrial robot, depending on the application. In this work, the DR burnishing process was carried out on a manual lathe.

Several theories [4,5,27–29] have been put forward to understand the LIE damage modes. These are water-hammer pressure, stress waves, radial wall jetting, and hydraulic penetration. Water-hammer pressure refers to the high pressure generated from the collision of high velocity water droplets with the target solid surface [27]. Water-hammer pressure leads to initiation of surface cracks. Repeated impacts develop stress concentrations in the solid specimen creating stress waves transmitting beneath the target surface until they interact with a discontinuity interface [27,28]. The stress waves reflect back and forth around the discontinuity interface, creating subsurface cracks which are caused due to the presence of tensile stresses. In the presence of pre-existing cracks, the radial wall jetting and hydraulic penetration modes play a main role in opening the cracks and removing the material under water droplet impingement conditions [27].

Thus far, LIE has been treated as a purely mechanical phenomenon [4]. LSP, SP, and LPB treatments are believed to enhance mechanical properties. However, LSP and SP methods did not show any improvement in the LIE performance of Ti64 [10,11]. This could be attributed to worsening the surface roughness of the treated specimen, which leads to decreasing the incubation period and the maximum erosion rate [30]. In contrast, DR treatment leads to smoother surfaces, which can be advantageous for improving the water droplet erosion behavior of Ti64. On the other hand, DR is expected to enhance the fatigue resistance of Ti64 specimens, because it results in larger magnitude and depth of residual stresses than other techniques. The effect of DR treatment on LIE performance of Ti64 has not been studied before. In this work, the LIE performance of the DR-treated Ti64 specimens, under different parameters of feed rate, spindle velocity, number of passes, and pressure, was extensively studied and compared to the LIE performance of the non-treated Ti64. Furthermore, the failure modes that occur during the different stages of the erosion process and their influence on the erosion rate were evaluated based on their logical order of occurrence.

2. Experimental Section

2.1. Materials

The Ti64 (AMS 4911) alloy was received as an annealed plate, with dimensions of $12 \times 12 \times 0.6250$ inch, from Performance Titanium Group (San Diego, CA, USA). Sixteen disks of

3″ diameter were machined and subsequently DR-treated. Two T-shaped DR samples (shown schematically in Figure 2) were cut out from each disk using waterjet cutting, to avoid inducing additional residual stresses. The edges of the T-shapes were chamfered, 15 °from the burnished surface, to remove the rough traces of the waterjet cuts, since they might act as crack initiators during the LIE test.
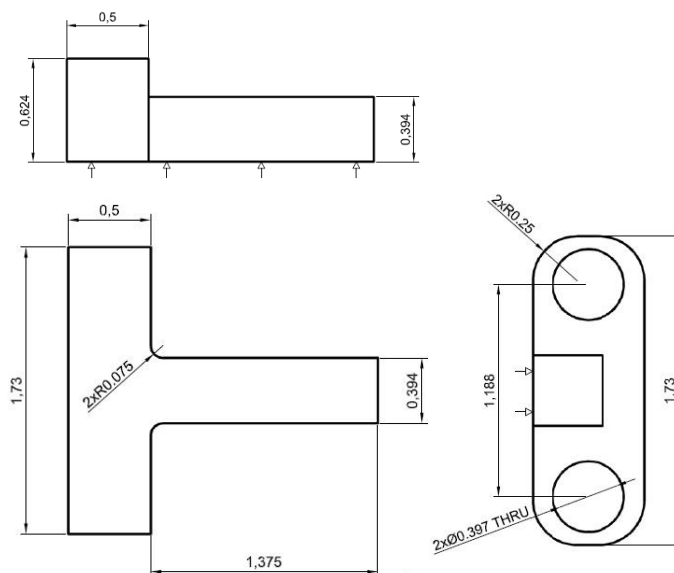

Figure 2. T-shape coupon used for LIE test. Dimensions are in inches. The arrows indicate the burnished surface.

2.2. Deep-Rolling Treatment

The deep-rolling tool was acquired from ECOROLL Company (Milford, OH, USA). The equipment consists of a 6.6 mm hard ceramic ball, able to process materials up to 65 HRC, equipped with a hydraulic pump that provides pressures up to 200 bar. DR treatment was carried out on a manual lathe using the DR tool to compress the surface of the rotating Ti64 disk that was held by the chuck. In the present work, several DR treatment parameters were varied in a two-level full-factorial (2k) design of experiments (DOE). These parameters are: spindle velocity, DR feed, number of passes, and DR pressure. Other parameters, such as DR ball material and diameter, were held constant. Each of the four selected parameters was utilized at two different levels, high (+) and low (−). The values of each level, listed in Table 1, were determined based on the available literature data [18,19] and recommended by ECOROLL. According to the DOE, DR conditions were developed and 16 Ti64 disks were treated using different conditions for each, as described in Table 2.

Table 1. Process parameters of DR-treated Ti64.

Level Parameters	High Level (+)	Low Level (−)
Spindle velocity (rpm)	150	75
DR feed (mm/r)	0.20	0.06
Number of passes	3	1
DR pressure (bar)	200	100

Table 2. Combination of parameters used for DR treatment of 16 samples.

Parameters	1	2	3	4	5	6	7	8	9	10	11	12	13	14	15	16
Spindle velocity	−	+	+	−	−	+	+	−	−	−	+	+	+	−	−	+
DRfeed	−	−	−	−	−	−	−	−	+	+	+	+	+	+	+	+
Number of passes	−	−	+	+	−	−	+	+	+	−	−	+	+	+	−	−
DRpressure	−	−	−	−	+	+	+	+	+	+	+	+	−	−	−	−

It is worth noting that the radial speed of the deep-rolling tool is changing along the tool path for the same spindle speed. Thus, the test specimens were prepared in a way that the LIE test is performed on the same radial distance for all coupons.

2.3. Characterization of DR-Treated Ti64

The surface roughness of the various burnished samples was determined by means of an electronic contact profilometer instrument (Mitutoyo Surftest SJ-210, Aurora, IL, USA). The arithmetic mean roughness (*Ra*) was used to represent the surface roughness. An average of five roughness measurements was taken for each sample.

A square-base pyramid-shaped indenter was used for Vickers surface microhardness testing. A nominal force of 100 gram-force (gf) and 15 s loading time were used. An average of five measurements was taken at the surface of each sample to evaluate the surface microhardness improvement after DR treatment.

The Incremental Hole Drilling method (IHD) was used to study the compressive residual stress distribution induced by the DR treatment. A strain gauge rosette, with three strain measuring grids ($0°$, $45°$ and $90°$: $\varepsilon_{0,45,90}$), is first bonded to the surface of the test specimen. A hole is then drilled, using a 1.5 mm diameter carbide-tipped drill bit driven by a high-speed air spindle with a rotational speed of 200,000 rpm, into the component through the center of the gauge. The original stress state in the component is calculated from the relieved strain values, according to ASTM E 837-01 [31].

The residual stresses were calculated from Hooke's law and the nominal strains, ε_n, were obtained from the bottom of the hole for each drilling step, depending on the surface strains value and a special transfer coefficients (correction curves), as thoroughly explained in [32]. From the directions of the three strain gauges, three residual stresses σ_0, σ_{45}, and σ_{90} can be calculated [33,34]. The main residual stresses ($\sigma_{1,2}$) and the main stress axes angle (α) can be determined by means of Mohr's circle, depending on the depth of the drilling. In this work, the depth increments were set at $4 \times 32 \ \mu m + 4 \times 64 \ \mu m + 8 \times 128 \ \mu m$, giving a completed hole depth of 1408 μm.

2.4. Liquid Impingement Erosion Test

The LIE test was performed using a horizontal rotating-disk water erosion rig shown schematically in Figure 3. The rig simulates the working conditions of the compressor blades and can reach a maximum testing speed of 500 m/s under vacuum. The rig has two camera ports, top and side, to observe the water droplet impingements using a Mikrotron high-speed camera (Munich, Germany). T-shape coupons, Figure 2, were tested using impact speeds of 250 and 350 m/s and initial water pressure

of 30 psi. The stand-off distance between the droplet generator and the test specimen was fixed at 50 mm for all LIE experiments.
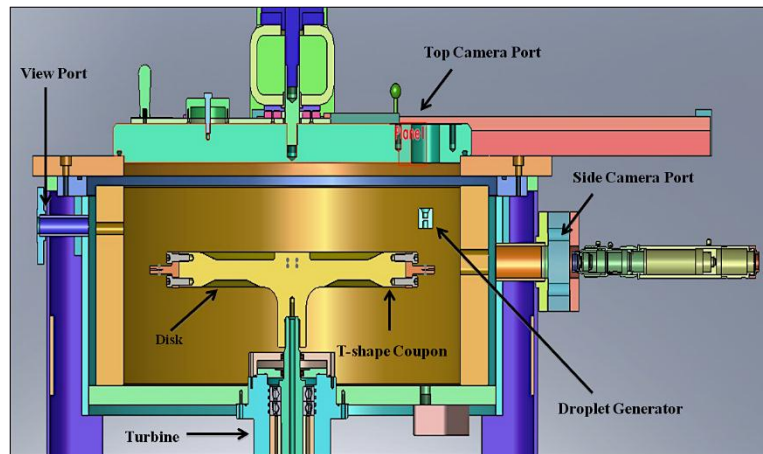

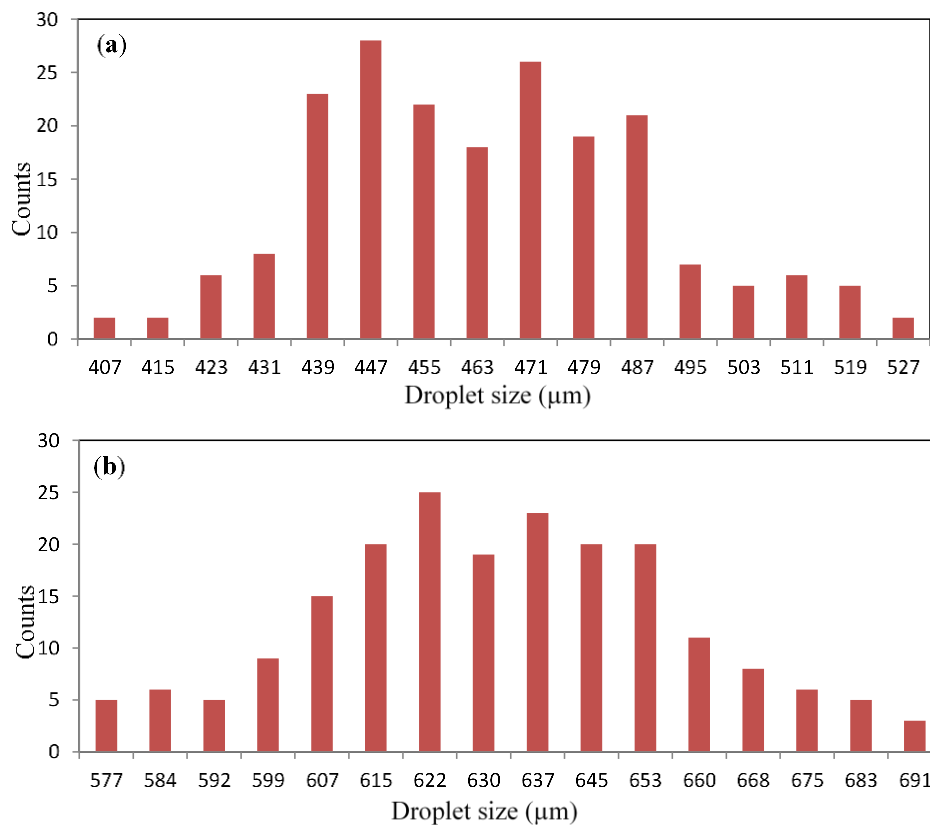**Figure 3.** Schematic illustration of the water erosion rig.

Figure 4. Droplet size distributions of (**a**) 400 μm; (**b**) 600 μm nozzles.

Two different nozzle sizes of 400 and 600 μm were used in the LIE tests to generate two different sizes of water droplets. The droplet size distributions for the 400 and 600 μm nozzles were measured using a high-speed camera (9000 fps) according to ASTM G73-10 [35]. The diameters of 200 droplets were measured from each nozzle. The water droplet size distributions for the 400 μm and 600 μm nozzles are shown in Figure 4a,b. The 400 μm nozzle generated droplet sizes with an average of 460 μm, while, for the 600 μm nozzle, the water droplet size has an average of 630 μm. The flow rates

of the generated droplets were 0.05 L/min and 0.1 L/min for the 400 μm and 600 μm nozzles, respectively.

3. Results and Discussion

In this section, a systematic study of the parametric effects contributing to the surface roughness, surface microhardness and residual stresses of DR-treated Ti64 was performed. Furthermore, the LIE performance of DR-treated Ti64 and the failure modes that occur during different erosion stages were evaluated.

3.1. Surface Roughness and Microhardness

One of the full-factorial methodology advantages over the one-factor-at-a-time experimental procedure is the ability to specify the interaction effect of several factors simultaneously. Pareto charts were used to represent the response of the parametric interaction on the DR process. The output of these charts could be affected by the chosen confidence interval (α), which is used to indicate the reliability of an estimate of the effects [13,36]. In the present work, a 5% of confidence interval (α) was used, which implies that 95% (1−α) of the confidence intervals would contain the true response. Accordingly, the influence of DR parameters on surface roughness and microhardness of Ti64 was determined.
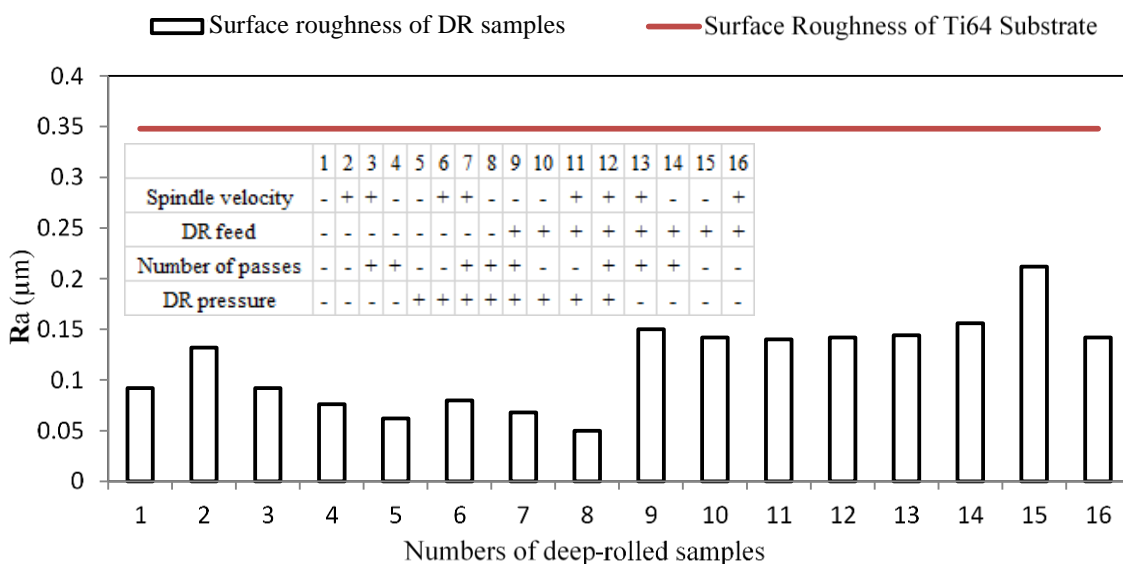

Figure 5. Surface roughness improvement of DR-treated Ti64. The surface roughness of the non-treated Ti64 is represented by a horizontal line at 0.35 μm. The DR parameters of the 16 samples are in the embedded legend and correspond to those in Table 2.

The effect of DR treatment on the surface roughness of the as-received Ti64 is shown in Figure 5. According to DOE analysis, the DR feed has the most dominant effect on the surface roughness of Ti64. An improvement of 0.072 μm in the surface finish of Ti64 could be achieved by decreasing the DR feed from 0.20 mm/rev (high level) to 0.06 mm/rev (low level). Moreover, DR feed shows a positive value according to DOE analysis, suggesting that the feed rate of the DR process is

proportional to the surface roughness. Hence, in order to minimize the surface roughness value, it is advisable to set the DR feed at a low level.

The same analyses were applied to the surface microhardness. The DR-treated Ti64 showed 10%−30% increase in surface microhardness. The DOE analysis showed that the interaction of the three parameters, feed rate, number of passes, and pressure, has the most significant effect on the surface microhardness. The effect of the three-factor interaction is inversely proportional (negative effect) to the magnitude of the surface microhardness, whereas the effect of the feed rate, alone, has a directly proportional effect (positive effect). The average microhardness values, shown in Figure 6, varied due to different DR process conditions.
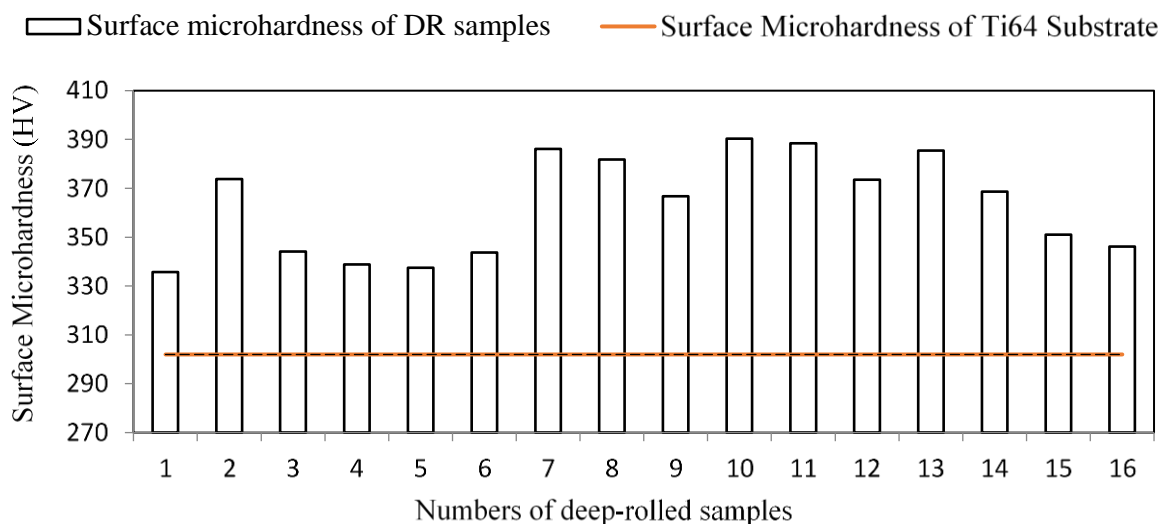
Figure 6. Comparison of the surface microhardness of DR-treated Ti64 with the non-treated Ti64. The microhardness of the non-treated Ti64 is represented by a horizontal line at 302 HV. The DR parameters of the 16 samples are in the embedded legend of Figure 5 and Table 2.

Figure 6 summarizes the microhardness results of the 16 DR burnished Ti64 specimens with various HV values. Comparing the HV values of deep-rolled samples #6 and #7 it is revealed that the HV value increased from 340 to 390 when changing the number of passes from one to three passes. These samples were chosen because the other three parameters (spindle velocity, DR feed, and DR pressure) were kept constant. This indicates that the HV values changed in response to the change in the processing parameters. Similar trend can be seen for deep-rolled samples #14 and #15 when the number of passes was changed.

It is interesting to note that increasing the pressure at low levels of feed rate decreases the surface microhardness but increases it at high feed rate when the other two factors are set at their low values, as illustrated in the response surface in Figure 7.

The values of the surface roughness and hardness of the reference Ti64, respectively, are presented as horizontal lines at 0.35 μm and 302 HV in Figures 5 and 6. This is because all references for the 16 DR tests were cut from the same Ti64 plate.
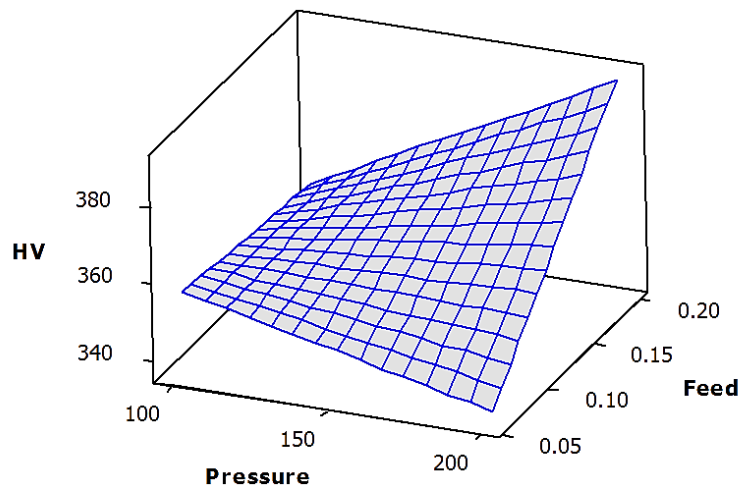
Figure 7. Response surface plot of microhardness *vs.* Feed and Pressure.

3.2. Residual Stress Profiles

Residual stress profiles revealed that the depth of the compressive residual stress layer, of the samples burnished at 200 bar DR pressure, ranged between 450 μm to 660 μm from the surface. For the same pressure, the magnitude of the maximum compressive residual stresses varied between 861 MPa to 1154 MPa, as shown in Figure 8. The depth of the compressive residual stress layer, for the samples burnished at 100 bar DR pressure, was between 288 μm to 448 μm from the surface, and the magnitude of the maximum compressive residual stresses ranged between 612 MPa and 889 MPa, as shown in Figure 9.
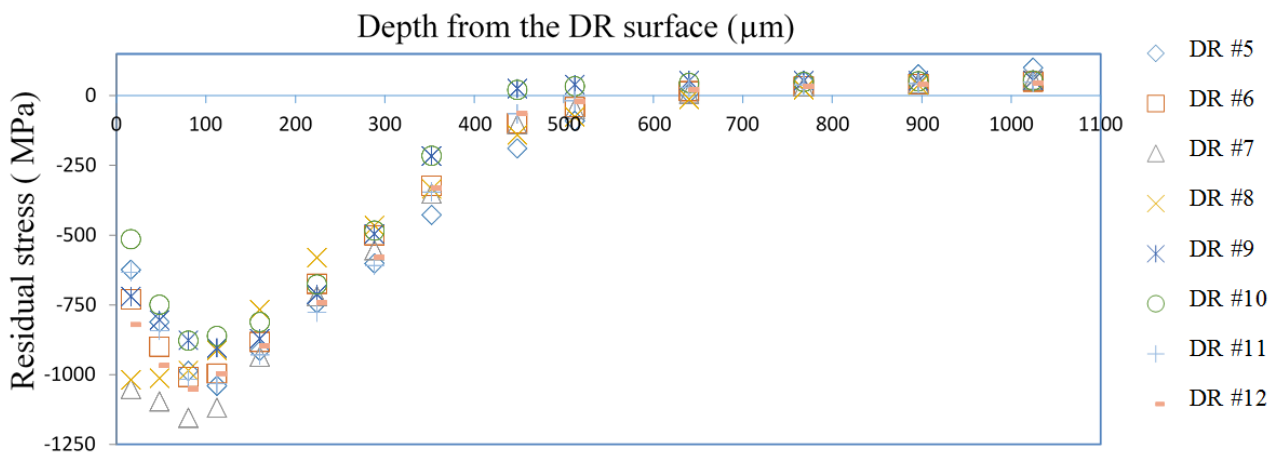

Figure 8. Residual stress distribution DR-treated Ti64 with 200 bar (high pressure).
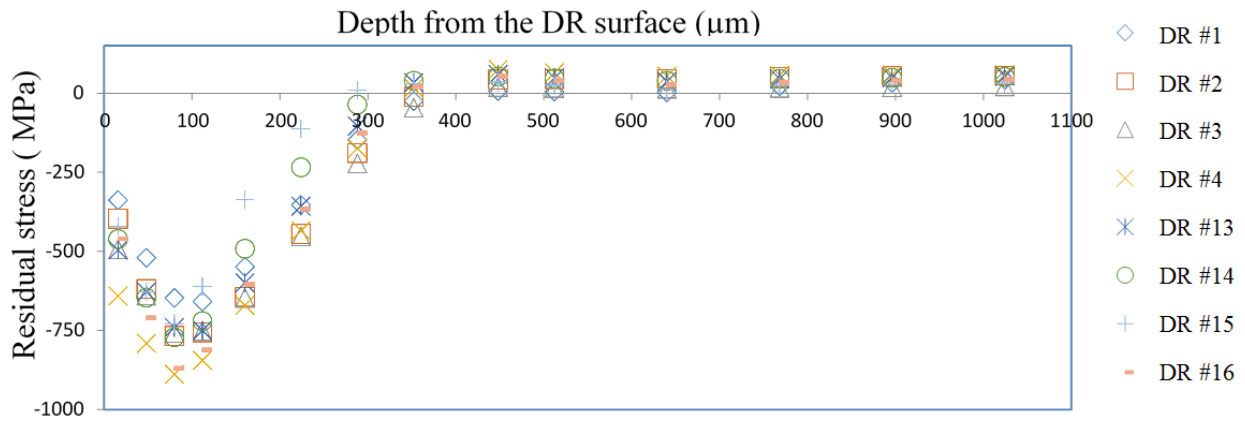
Figure 9. Residual stress distribution DR-treated Ti64 with 100 bar (low pressure).

The DR conditions that produce a deep and high magnitude of compressive residual stresses and low surface roughness and high microhardness values are used to test the LIE resistance of the burnished Ti64 alloy. Thus, samples DR #7 and DR #8 were chosen for the LIE tests. This selection is made in case the induced residual stress, due to deep-rolling, results in improvement of water erosion resistance, this effect will be most obvious in these two samples. The residual stresses measured on the surface of the non-treated Ti64 (reference materials) was ranging between ±150 Mpa. The non-treated Ti64 reference samples were polished down to an average surface roughness of 0.082 μm, which is a comparable roughness to the burnished samples in order to reduce the effect of surface roughness on water erosion resistance results. The DR processing parameters of the two selected samples and the non-treated Ti64 reference materials are summarized in Table 3.

Table 3. Summary of the DR processing parameters and experimental results of samples DR # 7 and 8 and reference Ti64.

Sample No.	DR #7	DR #8	Reference Ti64
Spindle speed (rpm)	150	75	-
Feed rate (mm/rev)	0.06	0.06	-
No. of passes	3	3	-
Pressure (Bar)	200	200	-
Surface Microhardness (HV)	381.06	381.78	302.0
Surface Roughness (μm)	0.068	0.050	0.082
Residual stresses (MPa)	−1154	−1018	Stress free
Depth of residual stresses (μm)	640	640	0

3.3. LIE Tests

Generally, the theoretical LIE curve shown in Figure 1 is characterized based on five stages: incubation, acceleration, maximum erosion, deceleration, and terminal erosion stage. However, it is more practical to represent the experimental LIE curve in three stages: incubation, maximum erosion rate, and terminal erosion rate, as shown in Figure 10. Determination of the five stages requires a large number of experimental points and it is very difficult to capture the acceleration stage.

Characterization of the nominal incubation period and maximum erosion rate are considered as the preferred evaluation method for presenting the LIE curves [4]. According to ASTM G73-10 [35], the

incubation period (A) is obtained from the interception of the straight line that best represents the maximum slope (B) with the *x*-axis, as shown in Figure 10. The maximum slope (B) represents the maximum erosion rate. Point (C) represents the *y*-axis intercept of the terminal erosion rate (D).

For each combination of LIE parameters (droplet size and impact speed), the tests were repeated twice to verify the consistency of the obtained results. The cumulative mass loss *versus* exposure time and number of impingements curves were plotted for all combinations. Table 4 summarizes the combinations of LIE test parameters and their experimental results.
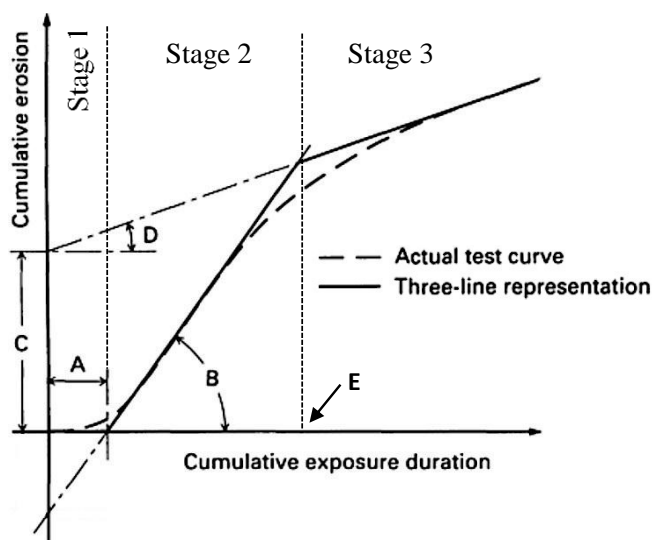
Figure 10. Maximum erosion rate determination methods, where, **A** is the nominal incubation period; **B** is the slope representing maximum erosion rate; **C** is the *y*-axis intercept of terminal erosion rate line; **D** represents the terminal erosion rate [4]; **E** is the end time of stage 2.

Table 4. The combination of LIE test parameters and experimental results of the LIE curve analysis.

Test No.	Impacting Speed (m/s)	Droplet Size (µm)	Samples	Incubation Period—A (min)	Maximum Erosion Rate—B (g/min)	End Time of the Second Stage of LIE—E (min)
1	250	460	DR #7	30	0.0002	94
			Ti64	29	0.0002	96
2	350	460	DR #7	3	0.0018	21
			Ti64	3	0.0018	21
			DR #8	3	0.0018	15
			Ti64	3	0.0018	15
3	250	630	DR #7	24	0.0002	121
			Ti64	28	0.0002	131
			DR #8	26	0.0002	88
			Ti64	25	0.0002	94
4	350	630	DR #7	1.5	0.0026	9
			Ti64	1.5	0.0026	9
			DR #8	1.5	0.0025	7
			Ti64	1.7	0.0025	7

In the following section, results of test #2 (Table 4) only are explained thoroughly, because all LIE test analyses were performed in the same way. LIE curves of both DR #7 and DR #8 samples with reference to untreated Ti64 are shown in Figure 11a,b, respectively.
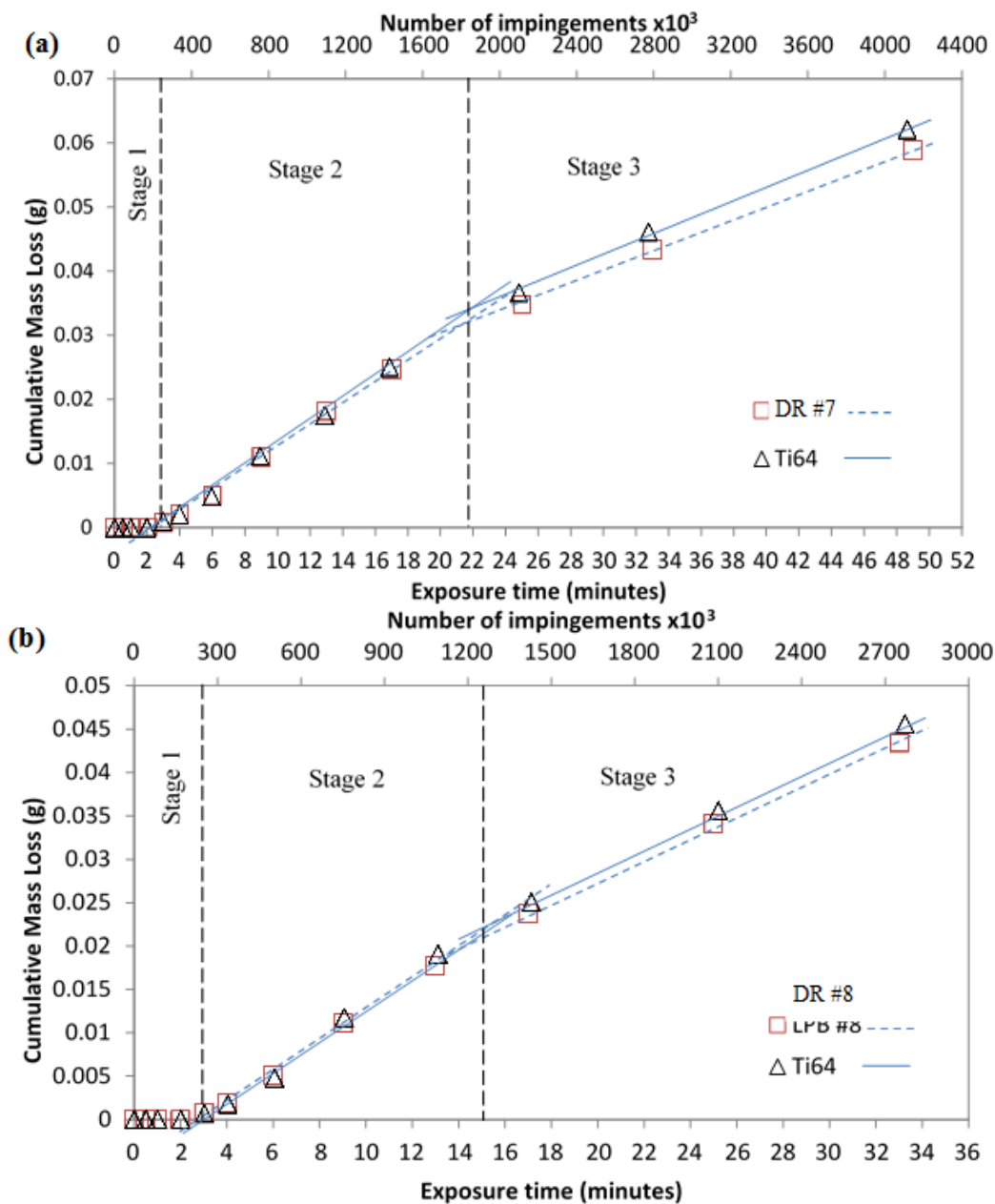

Figure 11. Erosion curves of (**a**) DR #7; and (**b**) DR #8 with reference Ti64 under 460 μm droplets and 350 m/s conditions.

In LIE test #2 (460 μm droplet size at impact speed of 350 m/s), both DR #7 and DR #8 samples, as well as the Ti64 reference sample, showed an incubation period (stage 1) of 3 min. Moreover, the trends in both figures did not show any variation in erosion rate as erosion evolves. The acceleration erosion stage (stage 2) ended after 21 min for DR #7/Ti64 test, and after 15 min for DR #8/Ti64. Erosion rates of all four samples increased to a maximum value of around 0.0018 g/min in stage 2 followed by a decrease in the erosion rate in stage 3. It is obvious from Table 4 that higher erosion rates occurred for the high speed and large droplet size tests.

The changes in the exposed surface of the tested samples at the same time interval during the LIE tests are shown in Figures 12 and 13. In both cases of the DR-treated and non-treated Ti64, the exposed surface showed no measurable material removal, but relatively shiny tracks due to the water droplet impingements during the incubation period (stage 1). Once the small pitting formed, the erosion rate started to increase, leading to formation of a crater and more material removal from other parts of the exposed surface. The craters coalesced as the erosion rate continuously increased in stage 2 and eventually resulted in the formation of the erosion line across the width of the exposed surface. Both the depth and the width of the crater were enlarged during the repeated impingements. The suggested LIE material removal mechanisms are explained in detail in the next section.
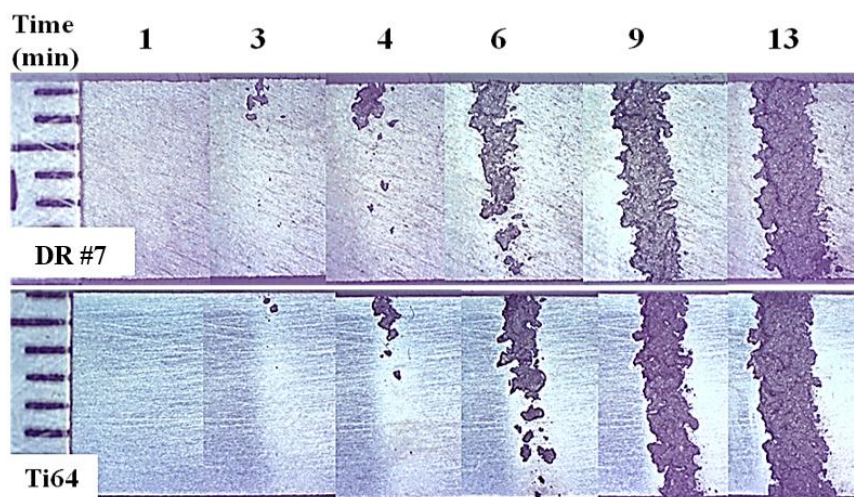

Figure 12. Macrographs of test 2 show the change in the exposed surface of DR #7 and non-treated Ti64 with time during the LIE test with 460 μm droplets at 350 m/s impact speed.
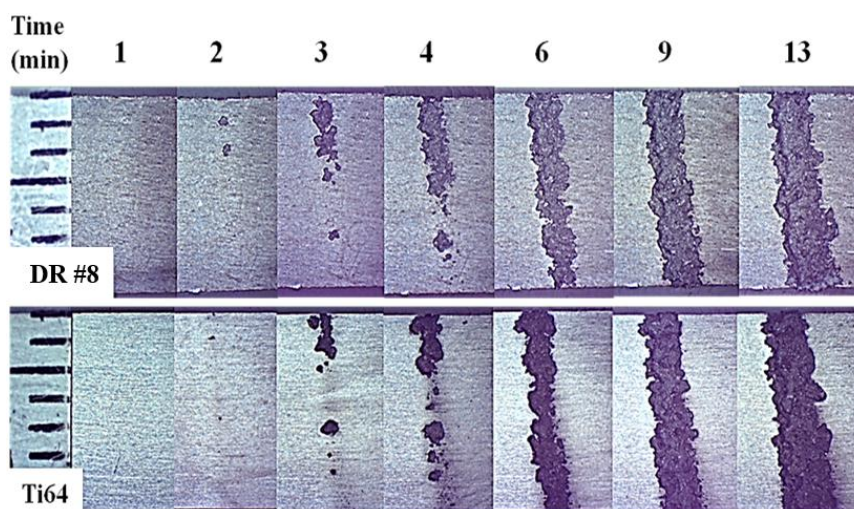

Figure 13. Macrographs of test 2 show the change in the exposed surface of DR #8 and non-treated Ti64 with time during the LIE with 460 μm droplets at 350 m/s impact speed.

Based on the LIE results (Table 4), it can be concluded that the DR-treated Ti64 samples showed little or no improvement in the LIE performance of Ti64 under the used test conditions. This can be

attributed to the strain hardening, making the material more brittle, and compressive residual stress mechanisms that balance each other due to the DR treatment.

3.4. LIE Material Removal Mechanisms

During the LIE tests, no significant difference between the erosion behavior of the DR-treated and the non-treated Ti64 samples can be observed. This is in agreement with previous studies [10,11], which reported that the mechanical surface treatments, such as shot peening and laser shock peening, are generally not effective for improving the water erosion resistance, although they are known for fatigue life improvement. This can be attributed to the fact that these treatments strain harden the material making it more brittle, which is additionally strain hardened, by the high-speed impacts of water droplets, which reduces the expected benefits obtained from the induced residual stresses in enhancing the LIE resistance. The effect of DR treatment on LIE performance of Ti64 has not been studied before. Thus, the present work aims to study the effect of the DR process parameters on the LIE performance of Ti64 specimens and to understand the failure modes occurring during different stages of LIE testing.
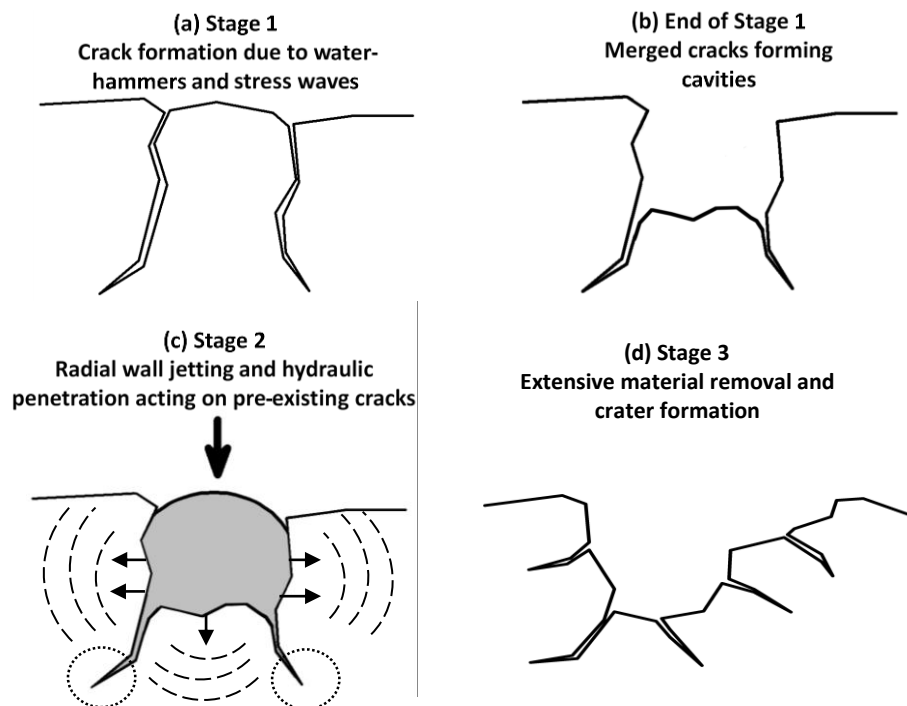

Figure 14. Schematic illustration of the material removal mechanism during LIE test. (**a**) Crack formation due to water-hammers and stress waves during Stage 1, (**b**) end of Stage 1 where cracks are merged and formed cavities, (**c**) radial wall jetting and hydraulic penetration representation in a pre-existing crack during Stage 2. The arrows represent the stress wave direction due to radial wall jetting, and the circles indicate the downward cracks propagation due to hydraulic penetration, (**d**) extensive material removal and crater formation in Stage 3.

In order to be able to explain the material removal mechanisms in the LIE test, the four damage modes illustrated schematically in Figure 14, must be well understood. Figure 14a represents the surface cracks developed due to water-hammer pressure and stress waves during stage 1. At the end of stage 1, Figure 14b,

cracks are merged and cavities are formed. Figure 14c represents the cavity horizontal expansion due to radial wall jetting, and the cracks travel forward into the depth due to hydraulic penetration. Figure 14d represents the material removal due to combination of the four modes.

When a water droplet hits a solid surface, two effects that damage the surface occur: high contact pressure and a subsequent liquid jetting outflow. The high-contact pressure is generated in the area of the impact; whereas, the subsequent jetting radiates out from the impacted area [4]. Consequently, the repeated liquid impacts on the solid surface generate stress waves travelling throughout the test specimen. Both modes, water hammer pressure and stress waves, are strongly responsible for initiating the surface micro-cracks in stage 1 of LIE test (Figure 14a). Figure 15 shows the micro-cracks initiated on the surface of the DR-treated Ti64 substrate, due to the combined effect of water hammer pressure and stress waves, in the initial stages of the LIE test.
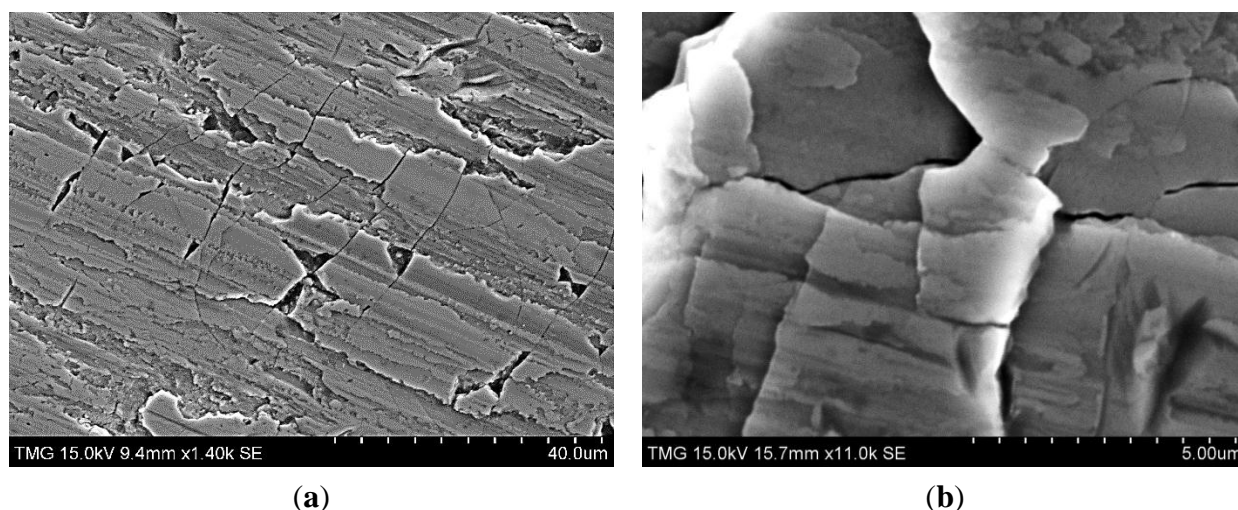

(**a**)   (**b**)

Figure 15. (**a**) and (**b**) Initiation of micro-cracks on the surface of the DR-treated Ti64 substrate due to the combined effect of water hammer pressure and compressive stress waves.

The stress waves travel in the solid substrate until they encounter a structural discontinuity, where part of the stress energy transmits through the discontinuity interface and the remaining part travels back as a reflected wave, as shown schematically in Figure 16. The compressive residual stress layer and/or nano-crystalline structure [13,36] of the DR-treated Ti64 represent discontinuity interfaces, indicated in Figure 16 as discontinuity #1. Thus, part of the stress waves transmits through discontinuity #1 and continues until it encounters the discontinuity #2, which might be the other end of the sample or another structural discontinuity, and reflects again, as shown in Figure 16b,c. As the LIE process evolves, the target surface is continuously impacted by the high-speed water droplets and the stress wave transmission and reflection takes place several times, leading to significant tensile stress at the discontinuity interface shown in Figure 16d, which propagates the existing cracks and initiates and opens sub-surface micro-cracks (Figures 14c and 17).

Figure 17a,b shows the sub-surface cracks that are initiated and propagated due to the cyclic tensile stresses in the vicinity of the structural discontinuity interface between α and β phases and at the end of the compressive residual stress layer (~640 μm) of DR #7 specimen.
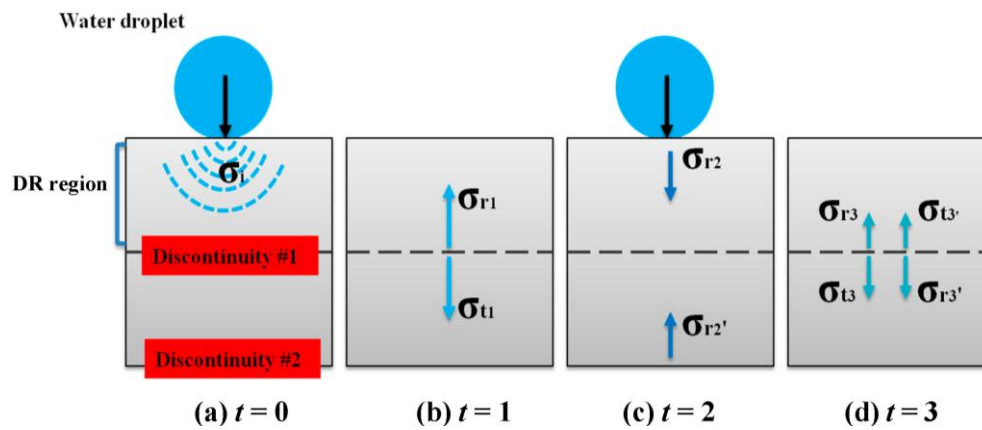
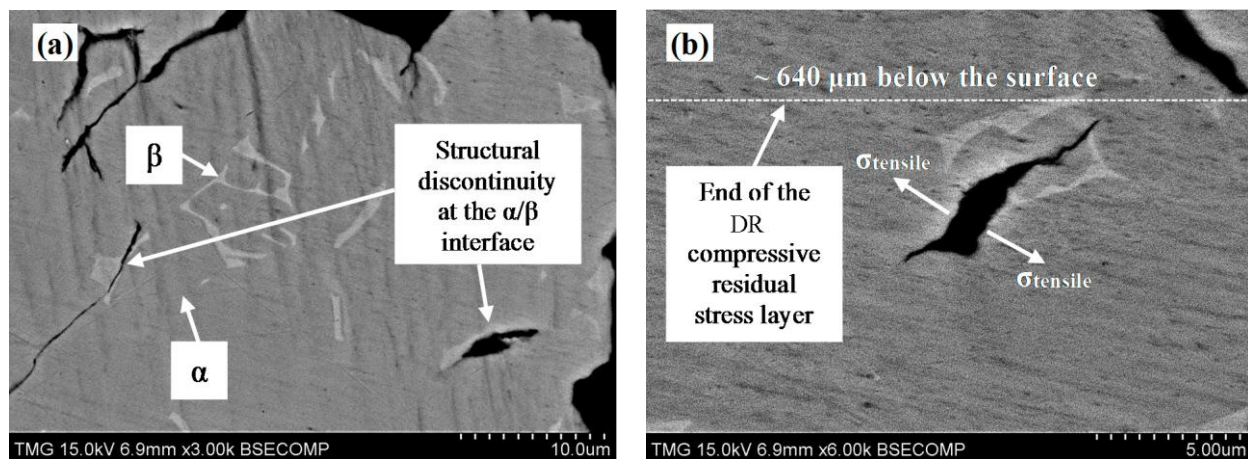**Figure 16.** Stress wave directions during LIE (*t* stands for time).

Figure 17. Initiation and propagation of the sub-surface micro-cracks due to the effect of the stress waves at (**a**) the α/β phase boundary; (**b**) end of the compressive residual stress layer.

Due to the dynamic generation of the water hammer pressure along the LIE test, the magnitude of the stress waves increases due to their interactions. Therefore, these two failure modes are simultaneously present in all stages of the LIE process. Stage 2 of LIE damage starts when the cracks reach a certain length and their lines merge together, forming isolated islands on the specimen's surface (Figure 15) and a network of micro-cracks underneath. At this point, cracks cannot go more in depth but their width increases due to the radial wall jetting effect. In this mode, the cracks turn into cavities due to the horizontal expansion of the cracks. On the other hand, the cracks travel forward into the depth, causing larger damages due to the hydraulic penetration mode, which takes place when large cavities are created. These two modes, radial wall jetting and hydraulic penetration, start acting on pre-existing cracks as illustrated schematically in Figure 14c.

In conclusion, the LIE stage 2 occurs due to the combination of the four damage modes: water hammer pressure, stress waves, radial wall jetting, and hydraulic penetration, as presented in Figure 18. In this stage, the erosion rate reaches its maximum value.
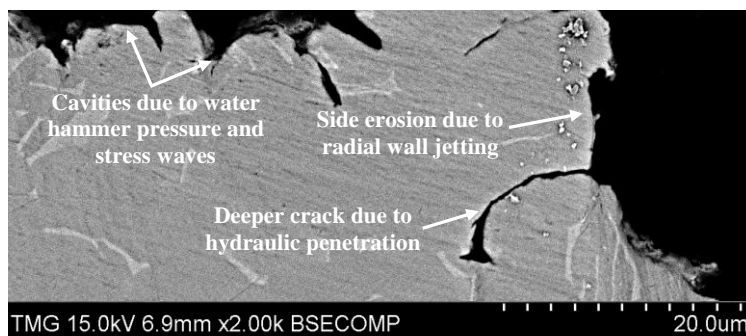
Figure 18. SEM micrograph shows the LIE damage of a DR-treated sample in stage 1 and 2 due to the combination of the water hammer pressure, stress waves, radial wall jetting and hydraulic penetration modes.

Stage 3 is defined as the terminal or steady-state erosion stage [4], where the erosion rate declines from its maximum value and remains approximately constant. Although in stage 3, the LIE damage is also characterized by the occurrence of the four damage modes as indicated earlier, radial wall jetting and hydraulic penetration play the main role in removing significant amount of the eroded material. Figure 19 shows an example of the LIE damage in stage 3, where the effect of the four damage modes is obvious from the amount of the removed material. The craters developed in stage 3 of the LIE test (Figure 19a) were deeper than those in stage 2 (Figure 18), and the erosion rate becomes steady in stage 3.
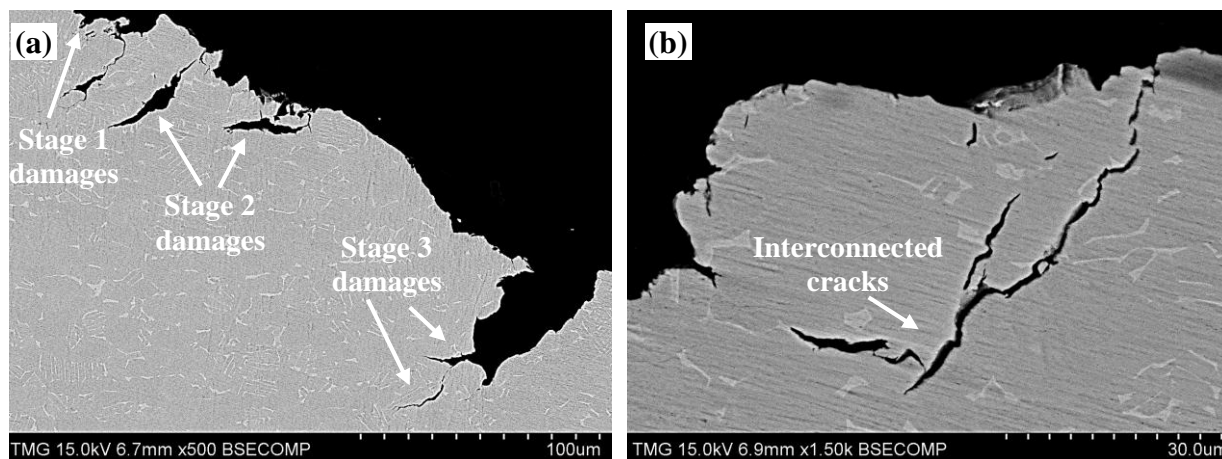

Figure 19. SEM micrographs of LIE damage in stage 3. (**a**) Represents the deep crater due to extensive material removal; (**b**) demonstrates the cracks connection around large portion of the eroded material.

3.5. Damage Behaviors of Ti64 before and after DR Treatment

3.5.1. Stage 1 of the LIE Test

Different features in stage 1 of LIE test between the DR-treated and non-treated Ti64 specimens were observed. The non-treated specimens, shown in Figure 20a, exhibits ductile behavior, which is an indication of the impact-damping capacity of the non-treated Ti64.
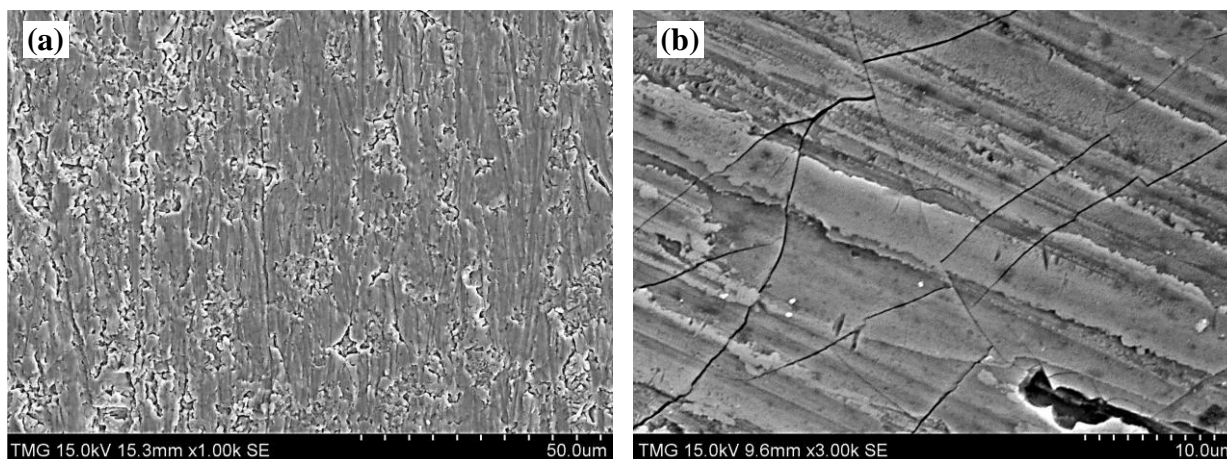
Figure 20. SEM micrograph of (**a**) non-treated Ti64 specimen; and (**b**) DR-treated Ti64 specimen during stage 1 of the LIE test.

The DR-treated specimens contained brittle features as shown in Figure 20b. This suggests that there are two competing mechanisms at the early stage of the erosion for DR-treated Ti64, which are the strain hardening and the compressive residual stress. The strain-hardened surface could decrease the erosion resistance due to the increased brittleness. However, the compressive residual stress layer is expecting to be beneficial for arresting the cracks that initiated at earlier stages of the erosion. These two mechanisms balance each other in the case of the DR-treated Ti64, which result in the same LIE behavior for both DR-treated and non-treated Ti64.

Although burnished samples were subject to three rolling passes that exert a high magnitude of plastic deformation on the specimen's surface, no cracks were observed prior the LIE test or in the un-impacted areas by water droplets. The cracks in Figures 15 and 20b were only observed during the LIE test. Thus, we concluded that these cracks were formed due to water droplet impacts.

3.5.2. Stage 2 of the LIE Test

The SEM micrographs of the tested Ti64 samples showed similar behavior to the surface roughening erosion mechanisms reported by Haag [37] at stage 2 of the LIE test. The untreated Ti64, Figure 21, shows the formation of surface slip bands, parallel to the side stress waves imposed by the radial wall jetting. The continuous water impacts result in folding the cavity boundaries under the influence of plastic deformation as shown in Figure 22.

In the case of DR-treated Ti64, different surface damage behavior, relative to the non-treated specimens, was observed. The surface of the DR-treated samples showed a more brittle behavior during stage 2 of the LIE test. Figure 23a shows the slip bands and their orientation relative to the side stress wave propagation. Unlike the case of the non-treated Ti64, the eroded surface shows a reduction of ductility due to the strain hardening induced by the DR treatment. The brittle features, then, turned into cracks as shown in Figure 23b. This can be attributed to the reduction of the impact damping capacity of the DR-treated surface due to the plastic deformation.
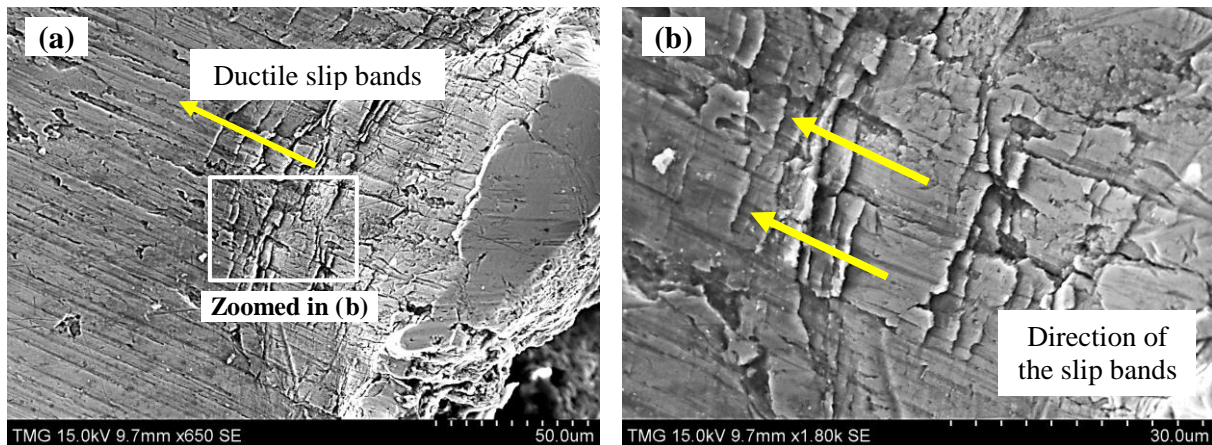
Figure 21. (**a**) and (**b**) SEM micrographs show ductile slip bands on the surface of the non-treated Ti64 specimen in the initial stages of LIE test.
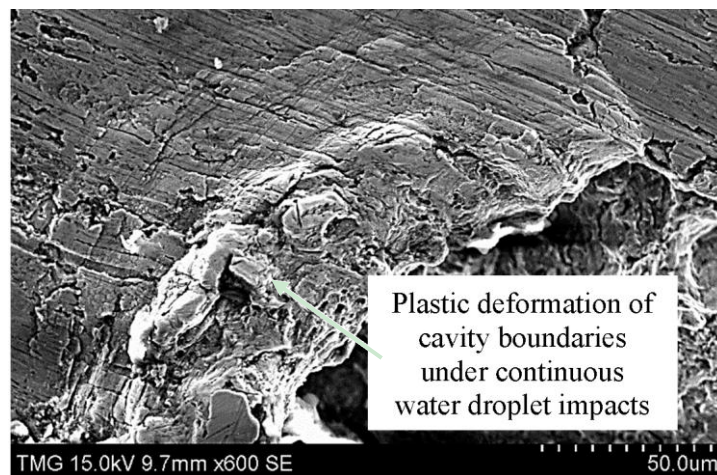

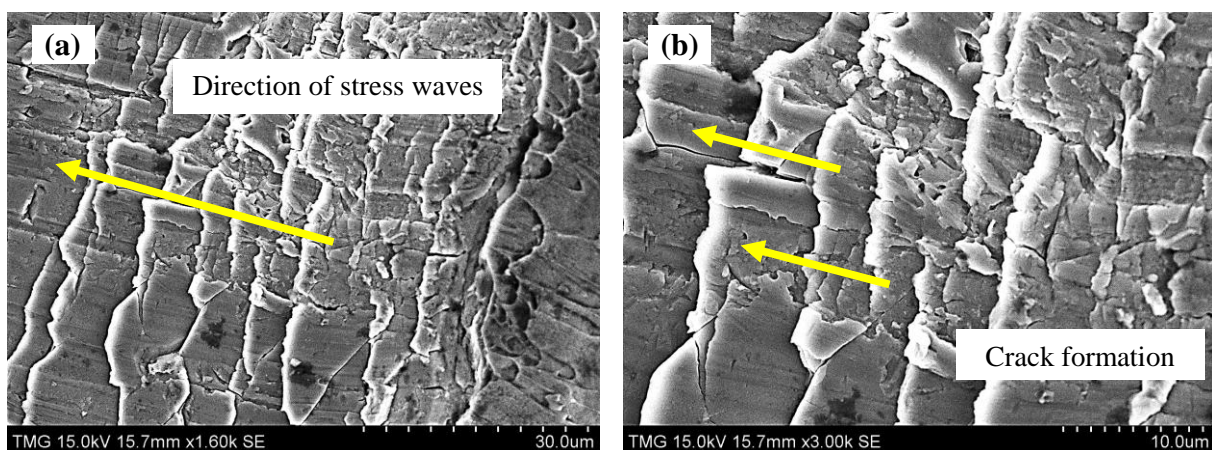**Figure 22.** SEM micrograph shows plastic deformation of the non-treated Ti64 surface.

Figure 23. Direction of stress waves and crack formation on the surface of DR-treated specimens at the initial stages of LIE test.

From Figures 21 and 23, different surface features were observed in stage 2 of the LIE test of the DR-treated and non-treated Ti64 specimens. The brittle features were not observed in the non-treated Ti64 samples, meaning that the fracture toughness of the DR-treated surface was reduced.

3.5.3. Stage 3 of LIE Test

The SEM micrographs of the initial damage on DR-treated and non-treated Ti64 samples under LIE test showed different features. However, later stages of their LIE damage exhibit very similar fracture behavior. This is due to the detachment of the thin hard layer, induced by DR treatment, during the initial erosion stages leaving, behind a bulk material of non-treated Ti64. The fracture behaviors of stage 3 are shown in Figure 24a,b.
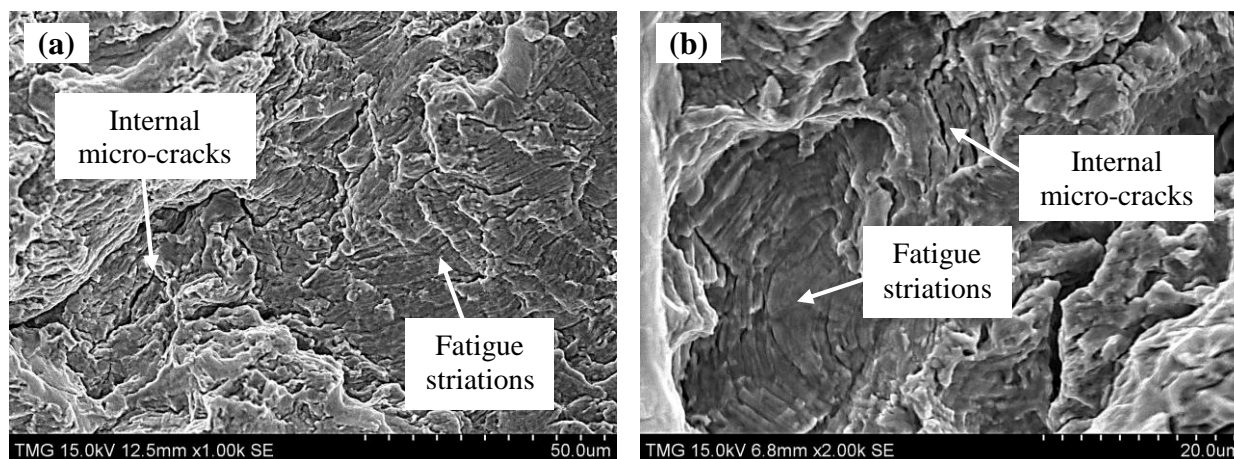

Figure 24. Fatigue striations in (**a**) non-treated Ti64; (**b**) DR-treated Ti64 samples.

Fatigue fracture usually occurs in LIE as a result of repeated water impacts and it is shown as a set of concentric ridges (fatigue striations) around the location of the water droplet impact sites. Luiset *et al.* [38] reported similar failure mode for stainless steel samples under erosion damage. Figure 24 shows the fatigue striations inside the erosion craters of both DR-treated and non-treated Ti64 samples.

Internal micro-cracks occurred due to the tensile stress at the discontinuity interface between α and β phases shown in Figure 17a, which resulted from the stress wave's propagation across the sample. The crack propagation is expected to move selectively along a weak path in the structure, which is normally the interface between different phases (α and β phases). This could be correlated to the erosion stage 2 as reported by Haag [37]. Similar behavior was also reported by Huang *et al.* [39] when studying water droplet erosion of Ti64. Kong *et al.* [27] reported that if imperfections are present at the grain boundaries, the material is more vulnerable to damage under water erosion. Kong *et al.* [27] reported that if imperfections are present at the grain boundaries, the material is more vulnerable to damage under water erosion. The triple grain split at the grain boundaries is schematically shown in Figure 25 [27]. Figure 25a assumes the presence of four grains attached at a random orientation, which simulates the feature observed in Figure 26a. The water droplet impacts produce a hammer pressure. This causes the detachment of grain no. 4 from the other three grains, producing a deep void as shown in Figure 25b. The same damage is observed in a real sample shown in Figure 26b.
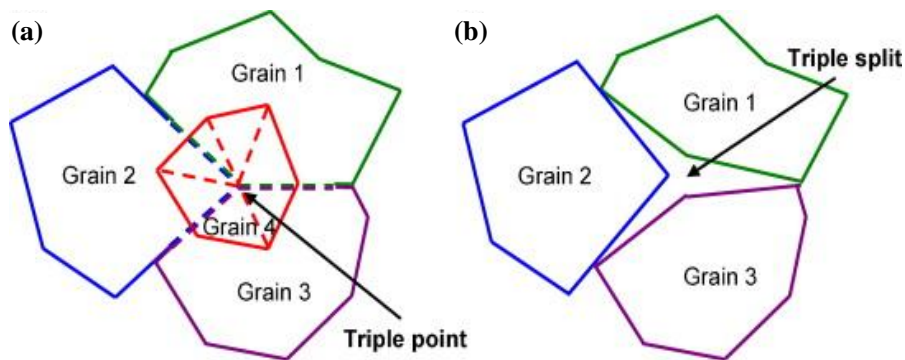
Figure 25. Illustration showing the triple damage failure (**a**) four grains structure; and (**b**) after losing grain No. 4 as a result of water hammer pressure [27].
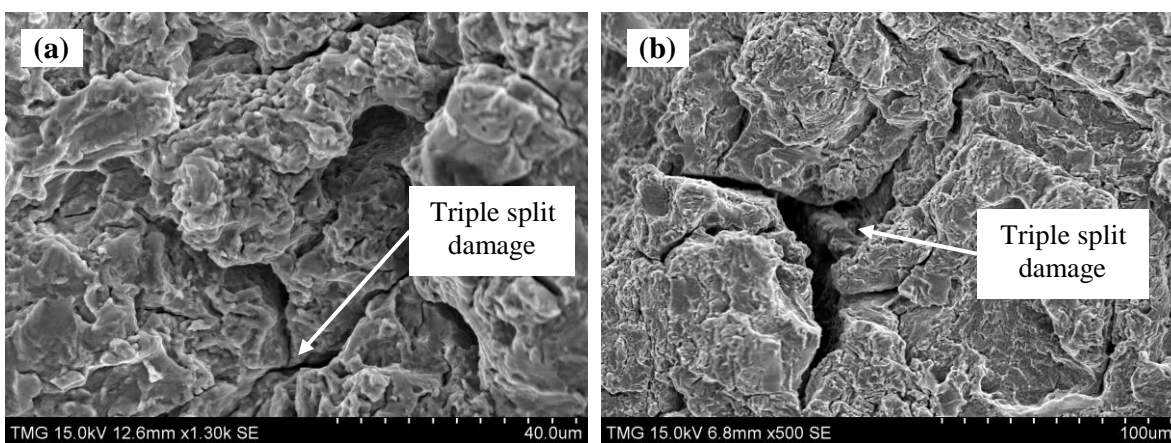

Figure 26. Triple split damage on (**a**) non-treated Ti64; and (**b**) DR-treated samples.

Other common features, between eroded DR-treated and non-treated Ti64 specimens, are ductile regions observed in the advanced erosion stages. Evidence is the existence of dimpled surfaces, which are an indication of ductile fracture as shown in Figure 27a,b for both DR-treated and non-treated Ti64 specimens, respectively. These dimples appear at the folded edges of the craters. The damage appearance in Figures 25b and 27b is an indication of full-grain detachment from the specimen contributing to the increased erosion rate in the third stage of erosion of the DR-treated samples.
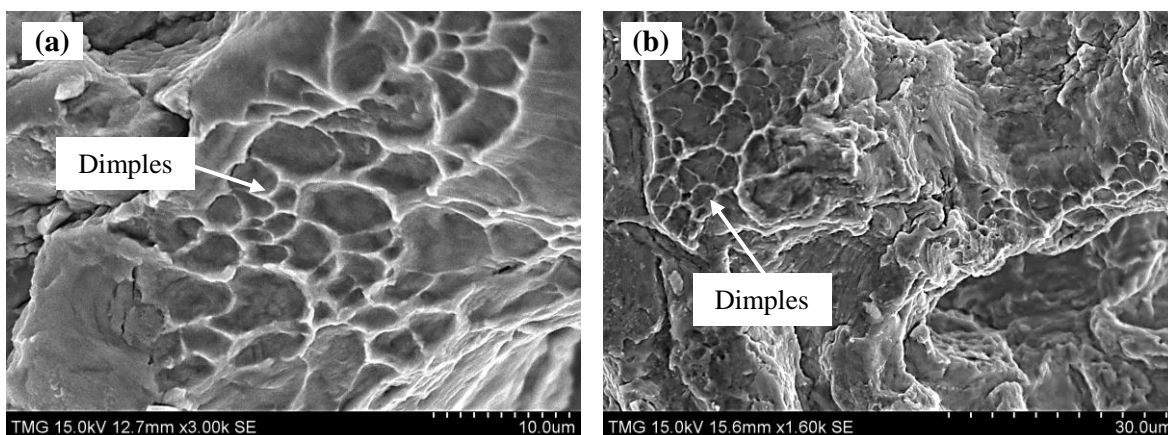

Figure 27. Dimples formation in the erosion crater for (**a**) non-treated Ti64 specimen; and for (**b**) DR-treated specimen.

4. Conclusions

A comparison between the LIE performance of DR-treated and non-treated Ti64 was performed. The DR-treated Ti64 samples showed little or no improvement in liquid erosion resistance at 250 m/s and 350 m/s impact speeds using 460 μm and 630 μm droplets. This could be due to the presence of two competing mechanisms: strain hardening and compressive residual stress that balance each other in the DR-treated Ti64.

Although LBP-treated and non-treated Ti64 showed similar LIE performance, both cases showed different damage modes. The present work characterized the first three stages of LIE, which are the incubation period, maximum erosion rate, and terminal erosion rate. A brittle fracture behavior was observed in the initial and intermediate erosion stages of the DR-treated Ti64, whereas the non-treated Ti64 showed a ductile fracture behavior. The damage mechanisms of DR-treated samples in the initial stages of the LIE test were observed to be in the form of micro-cracks nucleation, growth, and coalescence. These were observed to a lesser extent in the non-treated Ti64 samples, but the presence of slip bands and micro-deformations was dominant in this case. Nevertheless, advanced stages of damage for both DR and non-treated Ti64 samples exhibit very similar damage modes. The similarity in behavior can be attributed to the detachment of the DR-treated surface layer during the initial erosion stages. At advanced stages, the micro-cracks grow further along the interface of α and β phases. Moreover, the formation of dimples, fatigue-like failure, and large material removal were observed.

The four failure modes during LIE test, water hammer pressure, stress wave propagation, radial wall jetting and hydraulic penetration, were analyzed in detail. Water hammer pressure and stress waves modes were found prominent in all stages of the erosion damage, because they initiate and propagate cracks. The material removal process starts when the cracks are developed and after they have propagated until they coalesce, due to further liquid impacts. The radial wall jetting and hydraulic penetration modes start after cracking and pitting occur, causing further crack propagation and more material removal, especially in the intermediate and final stages of water erosion.

Acknowledgments

Author Contributions

Dina Ma was a Masters student who carried out the experiments, analyzed the results and wrote the initial draft of the paper. Ahmad Mostafa and Dmytro Kevorkov helped with the experiments and analyzing the results. Ahmad Mostafa revised the manuscript and prepared the final version of the paper. Pavel Jedrzejowski helped with initiation of the project and was the industrial lead on it. Martin Pugh co-supervised the student, discussed the results and revised the paper. Mamoun Medraj initiated and directed the project. He supervised the student, helped in the interpretation of the results, followed up on the progress step by step and revised the paper.

Conflicts of Interest

The authors declare no conflict of interest.

References

1. Meher-Homji, C.B.; Mee, T.R. Gas turbine power augmentation by fogging of inlet air. In Proceedings of the 28th Turbomachinery Symposium, College Station, TX, USA, September 1999; pp. 93–114.
2. Turbine inlet cooling: Technology overview. Available online: http://www.turbineinletcooling.org/ (accessed on 10 June 2015).
3. MDS coating technologies corporation. Available online: http://www.mdscoating.com/technology/index.html (accessed on 10 June 2015).
4. Heymann, F. *Liquid Impingement Erosion*; ASM International: Materials Park, OH, USA, 1992; Volume 18.
5. Rao, P.V.; Buckley, D.H. *Empirical Relations for Cavitation and Liquid Impingement Erosion Processes*; NASA Technical Paper 2339; NASA: Washington, DC, USA, 1984.
6. Jolliffe, K.H. The development of erosion damage in metals by repeated liquid droplet impacts. *Proc. A* **1968**, doi:10.1098/rspa.1968.0047.
7. Meng, P.; Geskin, E.S.; Leu, M.C.; Li, F.; Tismeneskiy, L. An Analytical and experimental study of cleaning with moving waterjets. *J. Manuf. Sci. Eng.* **1998**, *120*, 580–589.
8. Thomas, G.P.; Brunton, J.H. Drop impingement erosion of metals. *Proc. A* **1972**, doi:10.1098/rspa.1970.0022.
9. Xiong, J.; Koshizuka, S.; Sakai, M.; Ohshima, H. Investigation on droplet impingement erosion during steam generator tube failure accident. *Nucl. Eng. Des.* **2012**, *249*, 132–139.
10. Robinson, J.; Reed, R. Water droplet erosion of laser surface treated Ti6Al4V. *Wear* **1995**, *187*, 360–367.
11. Oka, Y.I.; Mihara, S.; Miyata, H. Effective parameters for erosion caused by water droplet impingement and applications to surface treatment technology. *Wear* **2007**, *263*, 386–394.
12. Zhuang, W.; Wicks, B. Mechanical surface treatment technologies for gas turbine engine components. *J. Eng. Gas Turbine Power* **2003**, *125*, 1021.
13. Nalla, R.; Altenberger, I.; Noster, U.; Liu, G.; Scholtes, B.; Ritchie, R. On the influence of mechanical surface treatments—Deep rolling and laser shock peening—On the fatigue behavior of Ti6Al4V at ambient and elevated temperatures. *Mater. Sci. Eng. A* **2003**, *355*, 216–230.
14. Gray, H.; Wagner, L.; Lütjering, G. Influence of shot peening induced surface roughness, residual macrostresses and dislocation density on the elevated temperature HCF-properties of Ti-alloys. In Proceedings of the 3rd International Conference on Shot Peening (ICSP3), Garmisch-Partenkirchen, Germany, September 1987; pp. 447–457.
15. Ludian, T.; Wagner, L. Mechanical surface treatments for improving fatigue behaviour in titanium alloys. *Adv. Mater. Sci.* **2008**, *8*, 44–52.

16. Prevé, P.; Hornbach, D.; Ravindranath, R. Application of low plasticity burnishing to improve damage tolerance of a Ti-6Al-4V first stage fan blade. In Proceedings of the 44th AIAA/ASME/ASCE/AHS Structures, Structural Dynamics & Materials Conference, Norfolk, VA, USA, 7–10 April 2003; pp. 1–9.

17. Prevéy, P.; Shepard, M.; Smith, P. The effect of low plasticity burnishing (LPB) on the HCF performance and FOD resistance of Ti-6Al-4V. In Proceedings of the 6th National Turbine Engine High Cycle Fatigue (HCF) Conference, Jacksonville, FL, USA, 5–8 March 2001; pp. 1–10.

18. Prevey, P.; Hornbach, D.; Cammett, J.; Ravindranath, R. Damage tolerance improvement of Ti-6-4 fan blades with low plasticity burnishing. In Proceedings of the 6th Joint FAA/DoD/NASA Aging Aircraft Conference, San Francisco, CA, USA, 16–19 September 2002; pp. 1–9.

19. Prevéy, P.; Hornbach, D.; Jacobs, T.; Ravindranath, R. Improved damage tolerance in titanium alloy fan blades with low plasticity burnishing. In Proceedings of the International Surface Engineering Conference, Columbus, OH, USA, 7–10 October 2002; pp. 1–9.

20. Jayaraman, N.; Hornbach, D.; Prevéy, P.; Langer K.; Hoover, J.; van Hoogan, S.; Shepard, M. Mitigation of fatigue and pre-cracking damage in aircraft structures through low plasticity burnishing (LPB). In Proceedings of the AISP, Palm Spring, CA, USA, 4–6 December 2007; pp. 1–11.

21. Prevéy, P.; Jayaraman, N.; Ravindranath, R. Fatigue life extension of steam turbine alloys using low plasticity burnishing (LPB). In Proceedings of the ASME Turbo Expo 2010: Power for Land, Sea, and Air, Glasgow, UK, 14–18 June 2010; Volume 7, pp. 2277–2287.

22. Zhang, P.; Lindemann, J. Effect of roller burnishing on the high cycle fatigue performance of the high-strength wrought magnesium alloy AZ80. *Scr. Mater.* **2005**, *52*, 1011–1015.

23. Ibrahim, A.A. An investigation into ball burnishing process of carbon steel on a lathe. In Proceedings of Al-Azhar Engineering Tenth International Conference, Cairo, Egypt, 24–26 December 2008.

24. Altenberger, I. Alternative Mechanical Surface Treatments—Microstructure, Residual Stresses and Fatigue Behaviour; In *Shot Peening*; Wagner, L., Ed.; Wiley-VCH: Garmisch-Partenkirchen,Germany, 2003; pp. 421–434.

25. Prevéy, P.; Jayaraman, N.; Cammett, J. Overview of low plasticity burnishing for mitigation of fatigue damage mechanisms. In Proceedings of the ICSP 9, Fatigue and Fracture of Steels, Paris, France, 6–9 September 2005; pp. 1–6.

26. Scheel, J.E.; Hornbach, D.J.; Prevey, P.S. Mitigation of stress corrosion cracking in nuclear weldments using low plasticity burnishing. In Proceedings of the 16th International Conference on Nuclear Engineering, ICONE16, ASME, Orlando, FL, USA, 11–15 May 2008; pp. 649–656.

27. Kong, M.C.; Axinte, D.; Voice, W. Aspects of material removal mechanism in plain waterjet milling on gamma titanium aluminide. *J. Mater. Process. Tech.* **2010**, *210*, 573–584.

28. Hammitt, F.; Heymann, F. *Liquid-Erosion Failures*; ASM International: Materials Park, OH, USA, 1986; pp. 164–171.

29. Adler, W.F. *The Mechanics of Liquid Impact*; Academic Press Inc.: London, UK, 1979.

30. Kirols, H.S.; Kevorkov, D.; Uihlein, A.; Medraj, M. The effect of initial surface roughness on water droplet erosion behavior. *Wear*, submitted for pubulication, 2015.

31. ASTM E837-01. *Standard Test Method for Determining Residual Stresses by the Hole-Drilling Strain-Gage Method*; ASTM International: West Conshohocken, PA, USA, 2001.

32. Schwarz, T.; Kockelmann, H.; Tietz, H.-D.; Böhm, S. *Eigenspannungen und Verzug Durch Wärmeeinwirkung (German)*; Wiley-VCH: Weinheim, Germany, 1999.

33. Wenzelburger, M.; López, D.; Gadow, R. Methods and application of residual stress analysis on thermally sprayed coatings and layer composites. *Surf. Coat. Technol.* **2006**, *201*, 1995–2001.

34. Residual stress and strain measurement (XRD and hole drilling). Available online: http://www.npl.co.uk/science-technology/engineered-materials/services/residual-stress-and-strain-measurement (accessed on 10 June 2015).

35. ASTM G73-10. *Standard Test Method for Liquid Impingement Erosion Using Rotating Apparatus*; ASTM International: West Conshohocken, PA, USA, 2010.

36. Maawad, E.; Brokmeier, H.-G.; Wagner, L.; Sano, Y.; Genzel, C. Investigation on the surface and near-surface characteristics of Ti–2.5Cu after various mechanical surface treatments. *Surf. Coat. Technol* **2011**, *205*, 3644–3650.

37. Haag, M. Untersuchungen zur schädigungsentwicklung an dampfturbinenwerkstoffen infolge von wassertropfenerosion. Ph.D. Thesis, Technische Universität Kaiserslautern, Kaiserslautern, Germany, 2012.

38. Luiset, B.; Sanchette, F.; Billard, A.; Schuster, D. Mechanisms of stainless steels erosion by water droplets. *Wear* **2013**, *303*, 459–464.

39. Huang, L.; Folkes, J.; Kinnell, P.; Shipway, P.H. Mechanisms of damage initiation in a titanium alloy subjected to water droplet impact during ultra-high pressure plain waterjet erosion. *J. Mater. Process. Tech.* **2012**, *212*, 1906–1915.